JPhys Materials

PURPOSE-LED PUBLISHING™

**PAPER** • **OPEN ACCESS**

# Insight into the magnetisation process of martensitic Ni–Mn–Ga films: a micromagnetic and vector magnetometry study

To cite this article: Francesca Casoli *et al* 2020 *J. Phys. Mater.* **3** 045003

View the article online for updates and enhancements.

You may also like

- X-ray imaging of spin currents and magnetisation dynamics at the nanoscale
Stefano Bonetti
- Model of spin accumulation and spin torque in spatially varying magnetisation structures: limitations of the micromagnetic approach
P Chureemart, I D'Amico and R W Chantrell
- Review on high-temperature superconducting trapped field magnets
Qi Wang, Hongye Zhang, Luning Hao et al.

This content was downloaded from IP address 150.146.130.245 on 09/01/2025 at 10:05

Journal of Physics: Materials

PAPER

# Insight into the magnetisation process of martensitic Ni–Mn–Ga films: a micromagnetic and vector magnetometry study

**Francesca Casoli**[1], **Gaspare Varvaro**[2], **Milad Takhsha Ghahfarokhi**[1], **Simone Fabbrici**[1] **and Franca Albertini**[1]

[1] IMEM—CNR, Parco Area delle Scienze 37/A, Parma 43124, Italy
[2] ISM—CNR, nM-Lab, Via Salaria km 29.300, Monterotondo Scalo, Roma 00015, Italy

**E-mail:** francesca.casoli@imem.cnr.it

**Keywords:** ferromagnetic shape memory alloys, $Ni_2MnGa$, magnetic thin films, micromagnetism, magnetisation process

Supplementary material for this article is available online

OPEN ACCESS

RECEIVED
5 June 2020

REVISED
5 August 2020

ACCEPTED FOR PUBLICATION
20 August 2020

PUBLISHED
8 September 2020

Original content from this work may be used under the terms of the Creative Commons Attribution 4.0 licence.

Any further distribution of this work must maintain attribution to the author(s) and the title of the work, journal citation and DOI.

## Abstract

This study investigates the magnetisation process of a martensitic Ni–Mn–Ga thin film with microstructure optimized to obtain a unidirectional and reversible magnetisation jump. The study has been realised by a thorough vector magnetometry characterisation and supported by micromagnetic modelling, considering different orientations of the applied field with respect to the symmetry directions of the sample. The model has been built on the film microstructure and experimental characteristics.

The main features of the magnetisation curves measured along the film symmetry directions can be well reproduced by the micromagnetic model, that is, neglecting structural and magnetostructural contributions to the free energy. The model also well reproduces the field-dependent behaviour of the transverse magnetisation components. The agreement demonstrates that the spatial organisation of magnetocrystalline anisotropy axes due to martensitic twinning has a dominant effect on the magnetisation process, giving rise to magnetisation jumps when the magnetic field is applied along the alignment direction of the twin boundaries. When a reverse field is applied along this direction, simulations show that magnetisation reversal proceeds through the formation and three-dimensional expansion of magnetic domains, passing around the zero field through a closed-flux domain configuration, with the domain walls showing perpendicular orientation of the magnetic moments.

## 1. Introduction

Magnetic shape memory compounds are among the most promising classes of materials for magnetic actuation and multiple-stimuli actuation, offering new capabilities to exploit in MEMS devices for information technology and automotive, or in soft robots for biomedicine, tissue engineering and aerospace [1–4]. Compared to a conventional shape-memory material, in which a huge elastic deformation is induced by temperature, in the magnetic counterpart the additional occurrence of magnetically ordered states and of a strong spin-lattice coupling also allows magnetically driven deformations [5–7].

At the origin of the magnetic shape memory effect is a magnetostructural transition from a high symmetry phase, stable at high temperature, to a lower symmetry phase, stable at lower temperature. In $Ni_2MnGa$, a model system within this class of compounds and the object of this work, the phase transition occurs from a cubic $L2_1$ phase (austenite) to a lower symmetry phase (martensite), which can show different crystal structures depending on compositional variations around the 2-1-1 stoichiometry [7–10].

The occurrence of the magnetic shape memory effect in Ni–Mn–Ga has been ascribed to two main phenomena: the *magnetic field-induced structural transformation* and the *magnetically induced reorientation of twin variants* (MIR) [7]. In the first phenomenon, the shape memory effect takes place when the martensite to austenite transformation is induced by a strong magnetic field [11, 12]. Differently, in the MIR

© 2020 The Author(s). Published by IOP Publishing Ltd

effect the reversible deformation of the material occurs due the motion of martensitic twin boundaries to favour the twin variants with easy magnetisation direction oriented parallel to the applied magnetic field [5, 13, 14]. The latter effect gives rise in single crystals to deformations up to 12%, much larger than the piezoelectric and magnetostrictive effects exploited in competing technologies [15].

The importance of magnetic shape memory thin films gains relevance for micro- and nano-scale devices, in which the direct integration of the thin film material offers clear advantages compared to the sizing and bonding of bulk single-crystals [1, 4, 16–19]. The capability to grow thin films with high structural quality and clear magnetostructural transition has been demonstrated by different authors [20–24]. The transition temperature values mostly depend on composition and film thickness, while the sharpness of the transition and thermal hysteresis are also related to structure quality and microstructural characteristics [22, 24–29]. After transforming to the martensitic phase, the thin film shows a complex pattern of twin variants and, depending on substrate/underlayer and film thickness, different types of twinning and different twin patterns have been observed [24, 26, 27, 30, 31]. The support of detailed XRD analyses and electron microscopy investigations (e.g. BSE, HRTEM) has been fundamental to disentangle the details of such complex patterns.

In previous works, the magnetisation curve measured in the martensitic phase as a function of an external magnetic field has been used to deduce the occurrence of the MIR effect in thin films, in analogy to what occurs in bulk materials, where the appearance of magnetisation jumps at definite field values marks the field-induced twin boundary motion that can be directly visualized by microscopy techniques [5, 32, 33]. Instead, visualizing twin boundary motion in thin films imposes major challenges on the experimental side, also due to the much smaller typical twin size. For this reason, the occurrence of the MIR effect in Ni–Mn–Ga films has been often deduced indirectly, mostly from the appearance of sudden slope variations in the first quadrant of the magnetisation curve [7, 23, 24, 26, 28, 34]. It has to be noted that this kind of slope variation is often associated to a specific type of twin microstructure: clear magnetisation jumps occur in thin films with full or partial Y-type twinning. Here, 'Y-type' refers to a specific orientation of the crystal cells within the twin variants and of the twinning planes with respect to the substrate symmetry directions, as originally defined in the paper by Diestel *et al* [35]. For this specific type of microstructure, Laptev and co-authors have demonstrated that micromagnetic simulations can give account of magnetisation jumps similar to those measured experimentally, raising doubts about the unconditional attribution of magnetisation jumps to the occurrence of the MIR effect [36]. Another kind of twinned microstructure occurring in thin films is X-type microstructure; micromagnetic modelling has been usefully employed to interpret the experimental results, here too, by simulating the MFM contrast in a Ni–Mn–Ga thin film [37]. Finally, by resorting to micromagnetic modelling, C Phatak *et al* could associate the appearance of nanoscale skyrmions in a thinned Ni–Mn–Ga crystal to the spatial modulation of magnetic anisotropy originating from martensitic twinning [38].

In our previous works, we have been able to grow epitaxial films with different twinned microstructures, thanks to the careful control of growth conditions and the application of external stimuli [26, 29, 39]. In this work, we focus on the magnetisation process of a martensitic thin film with microstructure optimized to obtain a unidirectional and reversible magnetisation jump. The study has been realised by an in-depth vector magnetometry characterisation, in which the longitudinal and transverse magnetisation components are measured, while applying the magnetic field along the symmetry directions of the film. The study is extensively supported by micromagnetic simulations. A micromagnetic model similar to those employed in [36–38] has been developed, but tailored to the specific thin film sample studied by magnetometry, in order to obtain the best possible correspondence between model and real sample. The model microstructure in fact reproduces the one observed in the thin film, *i.e.* a twinned microstructure with oriented Y-type twin boundaries. In addition, the experimentally measured characteristics have been introduced in the micromagnetic model. The comparison between measurements and simulations has been drawn for different experimental configurations, *i.e.* for the longitudinal and transverse magnetisation components obtained with magnetic field applied along the symmetry directions of the sample and at tilt angles to these directions, also analysing the three-dimensional evolution of the micromagnetic configurations as a function of field. Our paper presents and compares an extensive range of experimental and simulation results, allowing us to confirm and expand the conclusion of [36], also clarifying some of the doubts emerging due to the limits of the approaches previously adopted.

## 2. Experimental

### 2.1. Samples preparation and characterisation

Ni–Mn–Ga(200 nm)/Cr(50 nm) films were grown by RF sputtering on a single-crystal MgO substrate with (100) orientation. The films were grown in a system with a base pressure of $2 \times 10^{-6}$ Pa, setting the Ar pressure to 1.5 Pa and the growth temperature to 623 K. First, a Cr underlayer with 50 nm thickness was

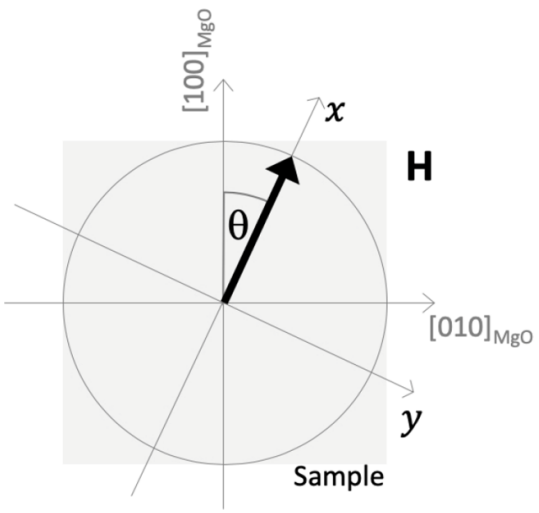


**Figure 1.** Schematic drawing of the vVSM measurement geometry. During the measurements the sample remains stationary, while the external field H rotates in the film plane. θ is the angle between H and the [100] MgO direction.

grown on top of MgO, by setting the voltage to 0.7 kV, thus obtaining a Cr sputtering rate of 0.02 nm $s^{-1}$. Then, the 200 nm Ni–Mn–Ga layer was grown with a voltage of 1.2 kV and a growth rate in the 0.10–0.11 nm $s^{-1}$ range. Film composition, as determined by energy dispersive x-ray spectroscopy, was in the $Ni_{53.7}Mn_{22.1}Ga_{24.2}$—$Ni_{52.0}Mn_{22.2}Ga_{25.8}$ range, as reported in our previous work [26].

Samples microstructure was studied by means of scanning electron microscopy (SEM, FEI Inspect—F) in both conventional and backscattered modes. The surface magnetic configuration was investigated by means of a Dimension 3100 atomic force microscope (AFM) equipped with Nanoscope IVa controller (Bruker Instrument). The surface topography was obtained in tapping mode, whereas magnetic domain images were acquired in tapping-lift mode with a lift scan height of 35–50 nm measured above topography.

A vector VSM magnetometer (vVSM, MicroSense Model 10) equipped with a rotating electromagnet ($\mu_0 H_{max} = 2$ T) and two sets of fixed pick-up coils perpendicular to each other was used to measure at room temperature (RT) the in-plane components of the magnetisation vector along the directions parallel, $M_x$, and perpendicular (transverse signal), $M_y$, to the external magnetic field $H$. The two directions $x$ and $y$ constitute a reference system that rotates with respect to the samples together with the field (figure 1). Comparing the parallel, $M_x$, and perpendicular (transverse signal), $M_y$, signals allows the evolution of the magnetisation vector to be investigated while sweeping the external magnetic field in the film plane, thus providing information about the magnetisation reversal mechanism.

### 2.2. Micromagnetic simulations

Micromagnetic simulations were performed by using the object oriented micromagnetic computational framework (OOMMF) code, where a time evolver that tracks the Landau–Lifshitz–Gilbert dynamics was implemented [40]. The material parameters used in the simulations were taken from our experimental data on Ni–Mn–Ga film and bulk samples [26, 41], except for the exchange stiffness constant $A$, which was deduced from a paper reporting on inelastic neutron scattering measurements performed on a bulk single crystal with composition $Ni_{50}Mn_{28}Ga_{22}$ [42]. The following values were used in the simulations: a saturation magnetisation $M_S$ of 490 kA $m^{-1}$, as measured by VSM on the thin film sample; a uniaxial second order anisotropy constant $K_1$ of $1 \times 10^5$ J $m^{-3}$, as evaluated by Singular Point Detection measurements on bulk polycrystals with composition similar to the film studied in the present paper (higher order anisotropy coefficients were neglected) [41]; an exchange stiffness constant $A$ of $5.07 \times 10^{-12}$ J $m^{-1}$ [42]. The geometrical distribution of magnetic easy axes in the sample was deduced from the microstructural and magnetic analyses reported in [26]. Micromagnetic simulations obtained on two different types of microstructural patterns will be presented in this paper, as explained in the 'results and discussion' and 'supplementary information' sections. In both cases, the model sample has a size of $1.2 \times 1.2$ $\mu m^2$, 200 nm thickness, a twin width of 25 nm (as deduced by SEM images) and a micromagnetic cell size of $5 \times 5 \times 5$ $nm^3$. Micromagnetic simulations were realized with field applied along the two edges of the MgO crystal, *i.e.* [100] and [010] directions, and along the diagonal of the basal plane of the MgO cubic lattice, *i.e.* [110] direction. For comparison with the vVSM experiments, micromagnetic simulations with field applied at small tilt angles to the [100] and [010] directions were performed, too. Due to the high computational

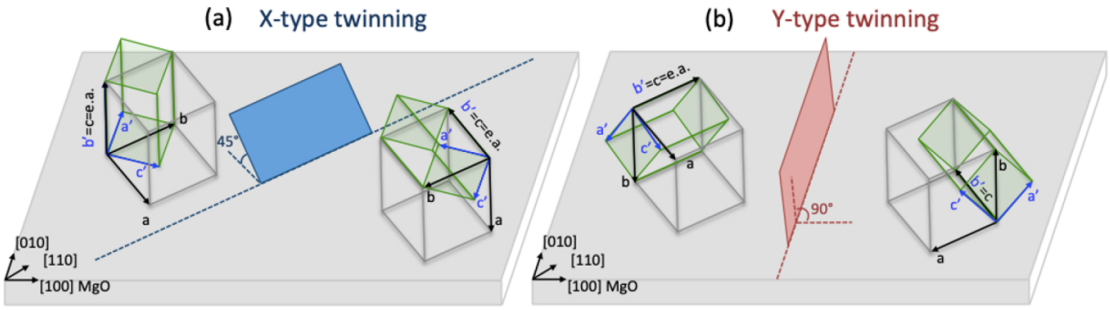


**Figure 2.** Sketches of the two different types of twinning occurring in Ni–Mn–Ga thin films: X-type (a) and Y-type (b). The grey and green boxes represent the crystallographic cell in the austenitic and monoclinic settings, respectively. Cell axes and symmetry directions of the MgO substrate crystal are represented by arrows. The unique axis $c = b$' is the easy axis of magnetisation (e.a.). Blue and red planes represent the twinning planes in the X-type and Y-type regions, respectively.

time, for each applied field direction only the first half of the hysteresis loop was simulated (from +2T to −2T), and the remaining part was obtained by symmetry.

## 3. Results and discussion

At RT the Ni–Mn–Ga films show a twinned martensitic microstructure, which forms on cooling the film grown at high temperature through the martensitic transformation temperature [26, 29]. At the growth temperature, the compound grows epitaxially in the $L2_1$ austenitic phase with epitaxial relationship $(001)[100]_{Ni–Mn–Ga}//(001)[100]_{Cr}//(001)[110]_{MgO}$. On cooling to RT, a structural transformation occurs from the austenitic to the martensitic structure, with a transformation temperature of approximately 335 K. The martensitic structure is twinned, as typically shown by ferromagnetic shape memory compounds, which accommodate the transformation stress with the formation of twin variants [24, 26, 27, 30, 31]. In general, these twin variants are organized into characteristic patterns, but the type of twinning and details of the twin variants pattern depend on the specific martensitic structure and on a complex balance between elastic, magnetic and magneto-elastic energy terms.

If we compare a thin film with a bulk crystal, we have to consider that the substrate constraint and surface energies influence the formation of twin variants [24]. It is also evident that magnetostatic energy, which in thin films is comparable in intensity to magnetocrystalline anisotropy energy, plays an important role in determining the twin variants pattern, due to the strong magneto-elastic coupling of the compound. Indeed, it has been demonstrated that in free-standing thin films the magnetostatic energy can drive a stray-field-induced shape memory effect [43].

Depending on the composition of the compound, the martensitic structure can be tetragonal, monoclinic (7M, 5M, non-modulated) or orthorhombic [7, 8]. In all these cases, the symmetry reduction determines an increase in magnetocrystalline anisotropy compared to the austenitic cubic phase. In our case, *i.e.* Ni–Mn–Ga thin films with Ni-rich composition grown on Cr/MgO(100), the structure is 7M-modulated monoclinic with lattice parameters $a' = 4.23$ Å, $b' = 5.52$ Å, $c' = 4.32$ Å and angle $\beta = 93°$. The cell parameters in the austenitic setting are the following: $a = 6.20$ Å, $b = 5.88$ Å, $c = 5.52$ Å with $\gamma = 91°$, with the $c$ axis corresponding to $b$' of the monoclinic setting. Two types of twinning can occur: X-type and Y-type [26, 35]. These are sketched in figure 2, both in the monoclinic and austenitic settings; for sake of simplicity, the latter setting will be preferred in the following description.

In X-type twins, the twinning planes are 101 planes and the short $c$-axis exchanges its orientation with $a$-axis, flipping from the in-plane to the out-of-plane directions, while the $b$-axis remains in the film plane. The $c$-axis is the easy magnetisation axis (e.a.) of the compound, as also observed in bulk materials with similar composition and the same crystal structure [26, 41].

In Y-type twins, which are also $a$-$c$ twins, the twinning planes are 110 planes and the $c$-axis switches between two symmetric in-plane directions, corresponding approximately to the diagonals of MgO basal plane, while the $b$-axis always remains perpendicular to the film plane (figure 2).

Interestingly, $a$-$c$ twins give rise to a typical microstructure with twin lamellae oriented at characteristic angles with respect to the film plane [30, 44]. This allows an easy identification of the specific type of twins by SEM and AFM [26]. X-type twins are oriented at 45° to the film plane and intersect the film surface along the [110] and [−110] MgO directions (figure 2). Y-type twins are oriented at 90° to the film plane and intersect the film surface along the [100] and [010] MgO directions (figure 2). Between the two types, only

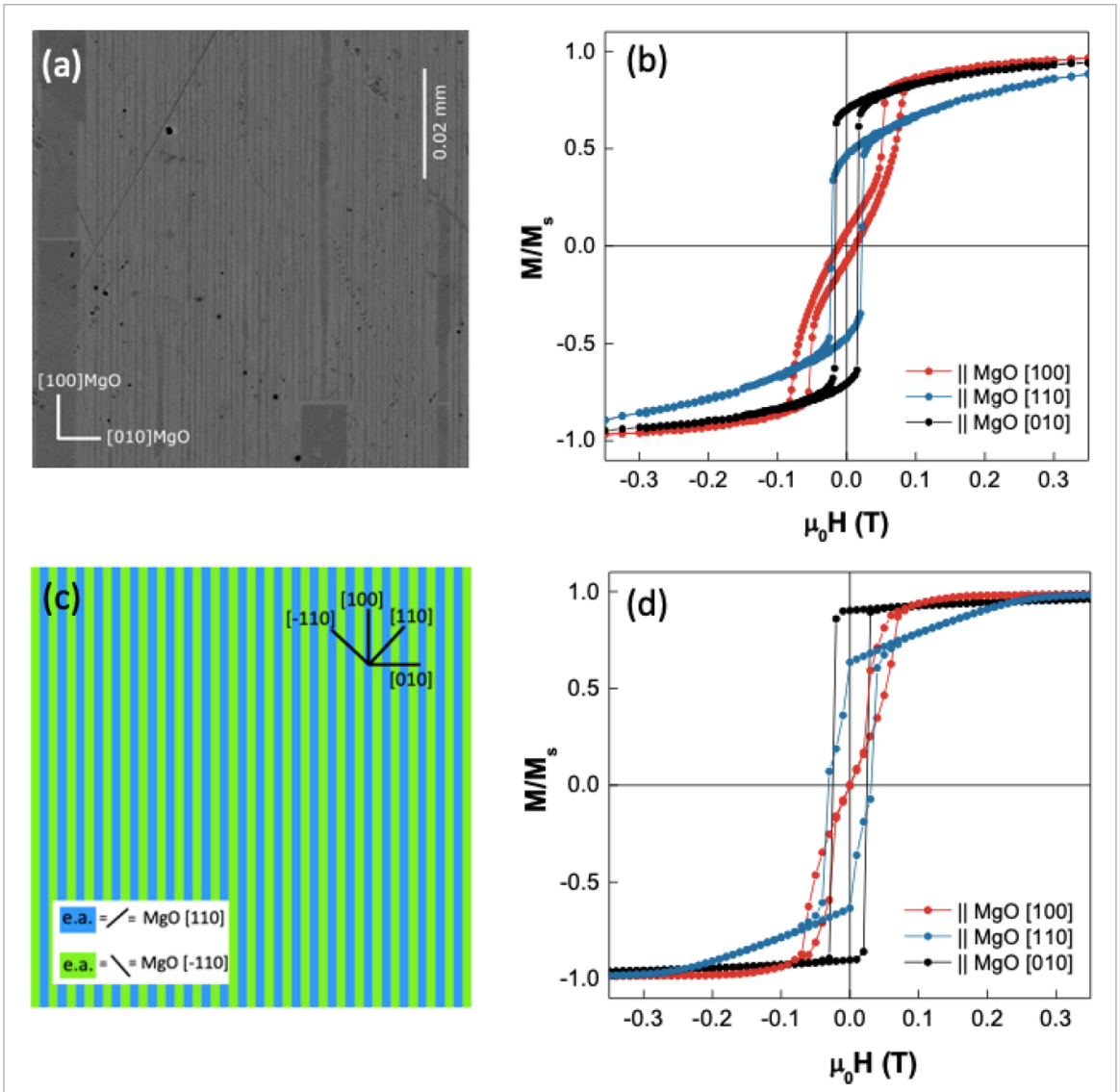


**Figure 3.** Microstructure and magnetisation curves of a Ni–Mn–Ga film with oriented Y-type twin boundaries: (a) large scale SEM image; (b) room temperature field-dependent magnetization loops along the three symmetry directions of the substrate crystal; (c) schematic drawing of the model sample used in the OOMMF simulation, alternating easy magnetisation axes (e.a.) along the two diagonals of the MgO crystal (green and light blue stripes are 25 nm wide); (d) hysteresis curves simulated by the OOMMF code with magnetic field applied along the same directions as in panel b.

X-type twins give rise to a surface corrugation and to a height contrast measurable by AFM, while both types of twin lamellae can be visualized in SEM images recorded by backscattered electron detector (BSE) [26, 30].

The two types of twin microstructure described above are energetically competitive for Ni–Mn–Ga films, and, depending on the substrate/underlayer, thickness and growth parameters, a full X-type, Y-type, or mixed X/Y-type film can be grown [26, 29, 31, 35, 37, 39]. Also a stress applied to the film during or after the growth can influence the microstructure, giving rise to specific orientations of the twin lamellae or inducing Y-type twins in a full X-type film [26, 39].

Figure 3(a) shows the X/Y microstructure of a film with Y-type twin boundaries oriented along one direction, that is, the [100] direction of the MgO substrate. We have been able to obtain such an oriented microstructure by applying a stress to the film during the growth [26]. Light stripes in the figure correspond to sample areas with Y-type twins, while dark areas correspond to X-type twins. The average width of the Y-type twin lamellae is 25 nm and a fraction of Y-type areas to X-type areas of 80% was estimated from large-scale SEM images, as reported in [26].

For the same thin film sample, the hysteresis loops measured along different directions of the MgO substrate are reported in figure 3(b). The easy-magnetisation direction of the system is parallel to the MgO [010] direction, while the [100] direction, *i.e.* the Y-type boundaries alignment direction, is the hard direction of the system. Along this latter direction, a sharp magnetisation jump was measured between 60 and 30 mT (values measured on the branch from +2T to −2T). The [010] and [100] MgO directions therefore

correspond to the maximum and minimum remanence values, respectively. Intermediate remanence values were measured along the [110] direction, which is the other symmetry direction of the system and corresponds to one of the two easy-magnetisation directions occurring in Y-type twins (figure 1 and [26]).

The occurrence of a magnetisation jump in the first quadrant of the magnetisation curves has been previously attributed, in analogy to what occurs in bulk single crystals, to the magnetic field induced reorientation of twin boundaries [5, 24, 26–28, 34]. In this phenomenon, moving the boundaries between neighbouring twins is more advantageous for the magnetic shape memory crystal than rotating the magnetisation of the system along the field direction, thanks to the high magnetocrystalline anisotropy and strong magneto-elastic coupling [5, 7, 13, 14]. Along with the twin boundary motion, an abrupt change of slope in the magnetisation curve occurs. On the other hand, twin boundary motion has been directly visualized in bulk single crystals [32, 33], while in thin films on substrate, also due to the much smaller typical twin sizes, it has never been directly observed to the best of our knowledge.

In order to understand the magnetisation process of the Ni–Mn–Ga film, we have realized micromagnetic simulations for a sample with distribution of the easy magnetisation axes as sketched in figure 3(c). Such a geometrical organization of the easy-magnetisation axes is the one imposed by Y-type twin variants, as described in figure 2(b). Our choice is justified by the experimental observation that Y-zones constitute the largest fraction of martensitic twin variants in the studied sample. The model sample is thus made of alternate stripes with easy-magnetisation axes along the [−110] (green) and [110] (light blue) directions of the MgO crystal, respectively. Stripe width corresponds to twin size. As described in the experimental section, compared to the approaches previously adopted, and in particular to [36], the magnetic and geometrical parameters used in the micromagnetic model were taken from our experimental data on the same thin film ($M_S$, thickness and twin size) or on bulk materials with similar composition (symmetry and value of the magnetocrystalline anisotropy). The exchange stiffness constant $A$ was deduced from a thorough study on inelastic neutron scattering measurements taken on a bulk sample with composition similar to our thin film [42]. Differently from [36], the organization of Y-type twins is in our case unidirectional and we have performed OOMMF simulations applying the magnetic field along all the symmetry directions of the sample.

The magnetisation curves simulated by applying the magnetic field along the three symmetry directions of the sample are reported in figure 3(d). The comparison between figures 3(b) and (d) evidences an excellent qualitative agreement between experimental data and simulations. Simulated magnetisation curves well reproduce the overall magnetic behaviour of the sample, with [010] and [100] directions representing easy and hard magnetisation directions for the system, respectively. The [110] direction shows an intermediate remanence value between the other two directions, both in the experimental and simulated curve. This direction corresponds to the easy-magnetisation $c$-axes of one-half of the model sample (light blue area in figure 3(c)), for the other half of the sample the easy-direction is oriented at 90° to the [110] direction, *i.e.* along the [−110] direction (green area in figure 3(c)).

The graphs in figure 4 represent the configurations of the micromagnetic moments at different steps of the reversal process, when applying the external field along the [100] direction, *i.e.* the 'jump' direction. The micromagnetic model indicates that the magnetisation reversal proceeds through the nucleation and growth of domains with resultant magnetisation along the positive and negative [010] directions and individual micromagnetic moments oriented along the local easy magnetisation directions, that is [110] and [−110] directions (figure 4(a)). At the positive field value of 160 mT, sample areas with resultant magnetisation oriented along the [010] direction are nucleated in the middle of the sample, *i.e.* at 100 nm from the bottom surface, and close to the sample edges. With decreasing the applied field value, these areas expand laterally and vertically, reaching the bottom and top surfaces at 50 mT. As visible in figure 4, on further decreasing the applied field value, magnetisation decreases due to the fast evolution of domain configuration and abruptly drops between 30 and 20 mT, when a closed flux configuration is reached, which is stable also at zero external field and for small negative field values. In this configuration, the areas with resultant magnetisation along the positive and negative [010] directions are separated by domain walls with moments oriented perpendicular to the film surface.

An animated gif image collecting the micromagnetic states of several points along the hysteresis loop is reported in the *supporting information* (figure S1 (available online at stacks.iop.org/JPMATER/3/045003/mmedia)).

The micromagnetic configuration at zero applied field gives an interpretation of the experimental results reported so far about the local magnetic configuration in Ni–Mn–Ga films with Y-type microstructure, as deduced by electron holography and MFM [26, 35]. In particular, magnetic microscopy measurements realized in the demagnetised state have been previously interpreted considering magnetic domains identical to the red and light-blue areas in the micromagnetic configurations in figure 4(a), separated by zigzag shaped 180° domain walls. Moreover, the domain walls appearing in the simulation explain the out-of-plane

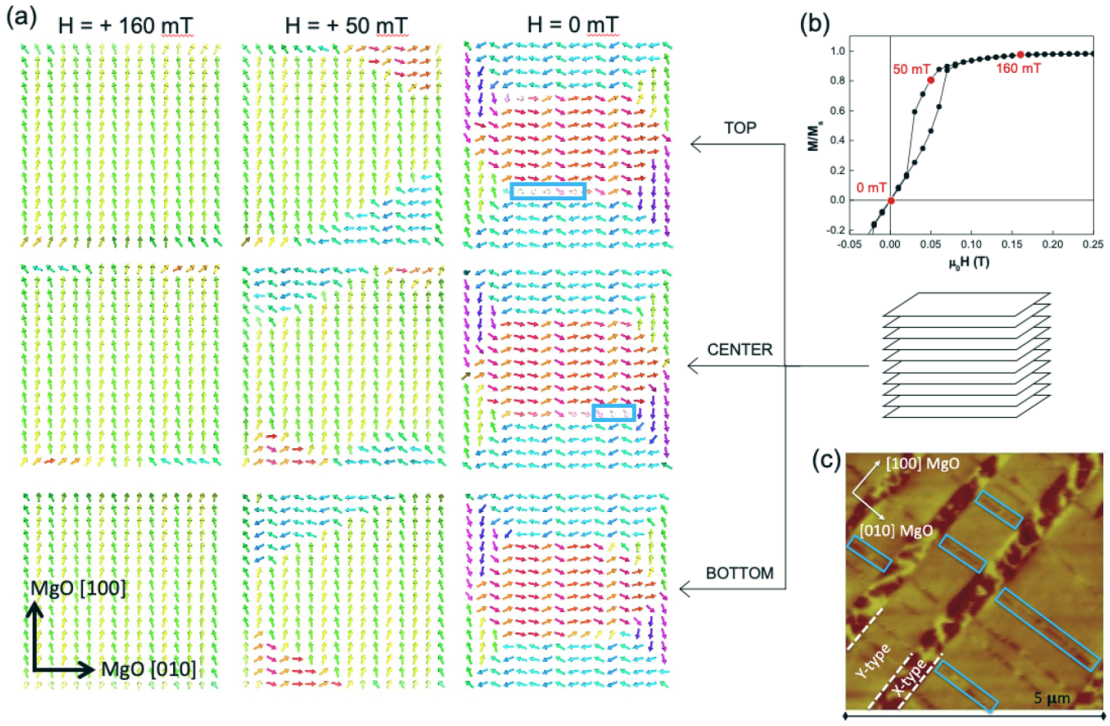


**Figure 4.** (a) Micromagnetic configurations during the magnetisation reversal process as obtained by the OOMMF simulation with external field along the [100] MgO direction. The results correspond to three different regions of the model sample, *i.e.* top surface, bottom surface and half thickness. Perpendicular domain walls are indicated by light blue rectangles. Configurations obtained for three representative values of the applied field are shown for each region. The same field values have been marked in the corresponding simulated magnetisation curve (b). (c) Magnetic force microscopy image of the sample in the demagnetised state; light blue rectangles indicate some of the out-of-plane magnetic domain walls, as in the corresponding areas marked in panel (a).

contrast measured by MFM in the narrow lines along the [010] direction. We have evidenced this contrast in the MFM image reported in figure 4(c), indicating some of the narrow lines with light blue rectangles; these domain walls separate magnetic domains with different resultant in plane orientations, as explained in detail in [26, 35]. Flux-closure domains instead (corresponding to purple and green areas in the micromagnetic configurations) have not been evidenced, to the best of our knowledge, in any experimental work so far. In the simulation these domains remain at zero field in order to minimize the magnetostatic energy in a sample with all Y-type microstructure, while in the experimental works, differently from the simulation, Y-type areas always border X-type areas, which might work as flux-closure zones.

Domain nucleation and expansion occur in the simulation in the field range 50–30 mT, which well corresponds to the experimental field range for the magnetisation jump. The good correspondence between the simulation and experimental measurements indicates that a purely magnetic domain nucleation and expansion process, and not only the field-induced twin boundary reorientation, can give account of the magnetisation jump.

No hysteresis is present in the central portion of the simulated curve, although irreversible processes clearly occur in the real system in the corresponding portion of the loop. In general, for the three symmetry directions of the system, the agreement between experiment and simulation with regard to the coercive field values is not perfect. The irreversibility of the magnetisation process is primarily influenced in the real system by microstructural defects, which are not taken into account in the micromagnetic model.

The difference between the measured and simulated $M_r/M_S$ values in the intermediate and easy magnetisation directions ($M_r/M_S^{[110]} = 0.5, 0.63$, $M_r/M_S^{[010]} = 0.75, 0.9$ for experimental and simulated curves, respectively) can be attributed to the simplicity of the model sample, characterized only by Y-type stripes of constant size that are perfectly aligned. Both the presence of misoriented easy-axes in the Y-type twin areas of the real sample and the contribution of X-type twin areas to the magnetisation process could determine the difference in simulated and measured $M_r/M_S$ values. X-type twin microstructure was not considered in the simulation for the following reasons. First of all, there is a large predominance of Y-type twin areas, corresponding to an areal fraction of 80% of the sample, as reported before. Typically, X-type films are spontaneously magnetised in the film plane, despite showing perpendicular stripe domains in MFM, which are weak stripe domains since for Ni–Mn–Ga films the quality factor $Q = 2K_1/\mu_0 M_S^2$ is less

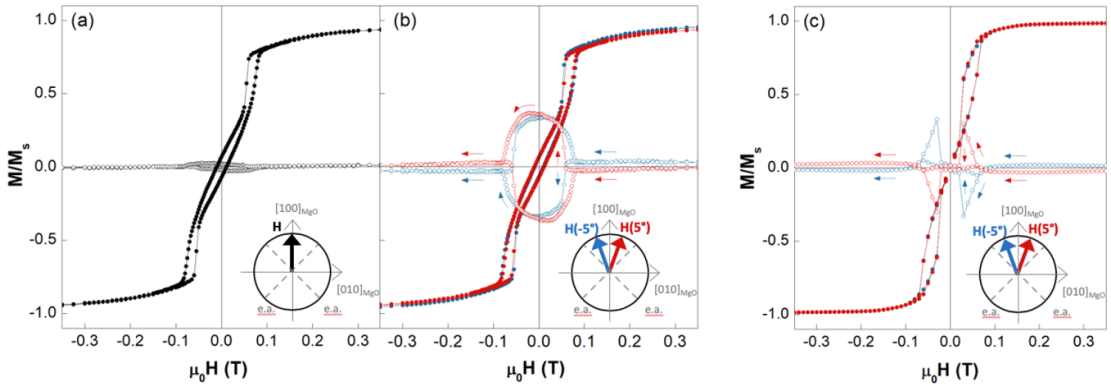


**Figure 5.** (a), (b) Experimental and (c) simulated field-dependent magnetisation loops collected in the film plane: (solid symbols) magnetisation component parallel to the external magnetic field H ($M_x/M_s$), (open symbols) transverse magnetisation component perpendicular to the external magnetic field H ($M_y/M_s$). (a) H is applied along the [100] MgO direction; (b), (c) H is applied at $+5°$ (red curve) and $-5°$ (blue curve) tilt angles to the [100] MgO direction. Insets: schematic drawing of the vVSM measurement and simulation geometry, the easy-axes—e.a.—(dashed line) are also indicated.

than 1 [29, 45]. All the in-plane directions are equivalently easy in an X-type film, coercive force and $M_r/M_S$ are around 10 mT and 0.2–0.3, respectively. Given these aspects, we can consider that in the sample under investigation the contribution of X-type areas, which superimposes to the dominant Y-type contribution, is isotropic with respect to the direction of the in-plane field. It is thus reasonable to conclude that, in the real sample, the contribution of X-type twins and of some degree of misorientation of the easy-axes also in Y-type twins, determine a small reduction in remanent magnetisation compared to an all Y-type sample with Y-type twins oriented along one direction.

As a further step towards understanding the details of the reversal process, the evolution of both the parallel and transverse components of the magnetisation vector were measured by using vector VSM magnetometry and the results were compared to the predictions of the micromagnetic model (see figure 1 for the measurement geometry). When the external field is applied along the hard [100] MgO direction (figure 5(a)), the transverse $M_y/M_s$ signal is close to zero in the whole $H$-range due to the symmetrical arrangement of the in-plane easy-axes with respect to the [100] MgO direction (insets in figure 5(a)). To break the symmetry, the same measurement was performed by applying the external field at an angle θ of $\pm5°$ to the [100] MgO direction (figure 5(b)). A structured transverse component emerges, the two curves measured at $-5°$ and $+5°$ being symmetric to each other as expected on the basis of the easy-axes configuration of the sample. The slight tilt of the external magnetic field does not affect the $M_x/M_s$ signal and then the overall magnetisation reversal mechanism, which was investigated by simultaneously studying the evolution of the $M_x$ and $M_y$ signals. To support the interpretation of the experimental data, micromagnetic simulations were performed under the same conditions, *i.e.* with the external field applied at angles $\theta = \pm5°$ to the [100] direction (figure 5(c)). The simulated $M_y/M_s$ signal is symmetric with respect to the [100] MgO direction and both the parallel and transverse components of the magnetisation present characteristic features that are in good agreement with the experimental data. The quality of the simulation is also confirmed by the agreement between experimental and simulated $M_x$ and $M_y$ curves collected with the external field applied along different directions as described in the *supporting information* (figures S2 and S3). The main difference between the experimental and simulated curves concerns the trend of the $M_x$ and $M_y$ signals in the central portion of the loop, where irreversible processes occur in the real system, while a fully reversible behaviour is observed in the simulated curves. With a tilt of $+5°$, starting from the positive saturated state, the rapid increase of $M_y$ in correspondence to the abrupt drop of the $M_x$ signal is followed by a sudden decrease of the $M_y$ signal to a negligible value in the simulated curve, while it remains almost constant in the experimental loop before dropping in correspondence of the steep increase of the $M_x$ signal in the opposite direction. This discrepancy, as better discussed later in the text, is likely a consequence of the presence of inhomogeneities in the real system that cause irreversible processes in the central portion of the loop.

To analyse in detail the reversal mechanism, we focused on the simulated and experimental curves collected at $\theta = +5°$. Figure 6 shows the micromagnetic configuration states of representative points in the simulated field-dependent magnetisation loops. Similarly to the case where the field is applied along the [100] MgO direction (figure 4), the micromagnetic simulations indicate that the magnetization reversal proceeds through the nucleation and evolution of transverse domains (point *II*), then creating a closed-flux configuration (point *III*) that gradually evolves (central part of the loop) until the external field $H$ is large enough to drive a rapid growth of domains oriented along the negative MgO [100] direction (around point

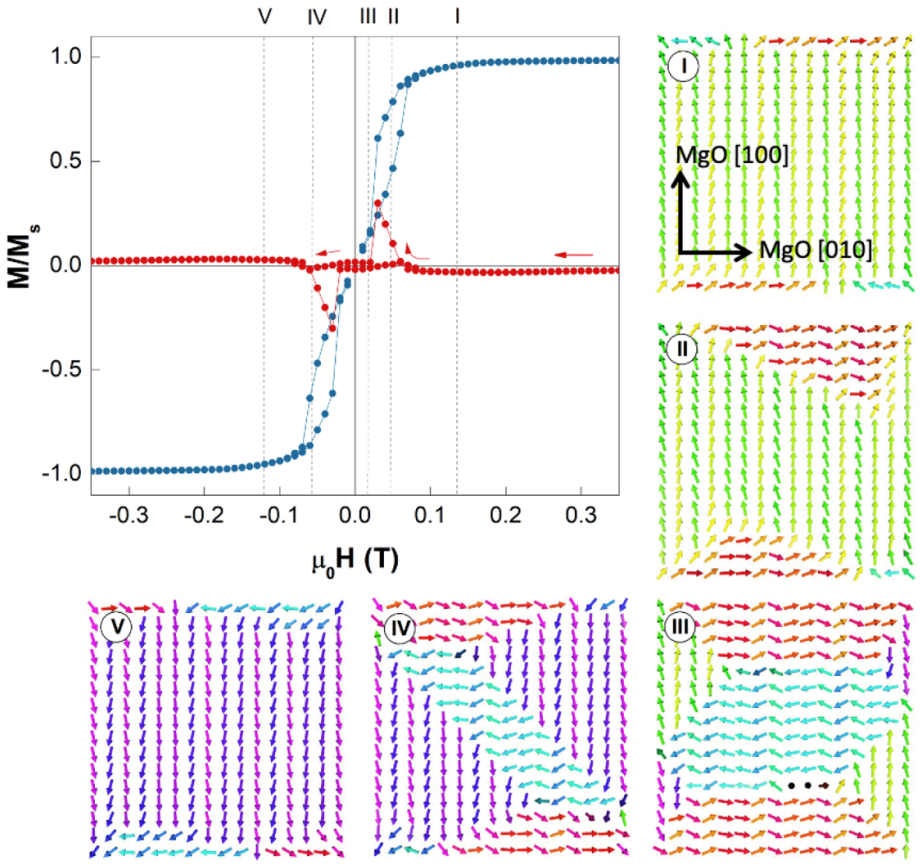


**Figure 6.** Micromagnetic configurations at half thickness corresponding to representative points in the simulated loops ($M_x/M_s$: blue curve; $M_y/M_s$: red curve) obtained with the external field at an angle $\theta = +5°$ with respect to the MgO [100] axis.

*IV*). The latter domains become dominant (point *V*) while the field is further increased towards the saturation point. Compared to the simulation reported in figure 4, the nucleated transverse domains are now oriented along the positive [010] MgO direction owing to the tilting of external field toward the same direction.

A comprehensive explanation of the reversal mechanism in the real system was elaborated by analysing the experimental $M_x$ and $M_y$ signals on the basis of the simulation results, which indicate the formation of magnetic domains whose resultant magnetization is oriented along the [100] and [010] MgO directions. Simple trigonometric considerations were used to deduce, for representative field values, the magnetic domain configuration that best explains the measured values of $M_x$ and $M_y$, while being consistent with the indications provided by the micromagnetic simulations. These results are reported in figure 7 for representative points in the magnetization loops of the upper panel: the middle panel shows qualitative sketches of the magnetization components along the [100] and [010] MgO directions; the bottom panel shows the corresponding schematic pictures of the magnetic domain configurations.

When the system is fully saturated under a positive external field, all the magnetic moments are aligned along the field direction, *i.e.* $M_x/M_s = 1$ and $M_y/M_s = 0$. As the field magnitude is progressively reduced, the magnetic moments start to rotate towards the [100] MgO direction to minimize the system energy (as the position is symmetric with respect to the easy axis directions), thus explaining the reduction of the $M_x/M_s$ signal and the slight increase of the $M_y/M_s$ component in the negative direction (point *I*). The following abrupt reduction of the $M_x/M_s$ signal, and the corresponding steep increase of the $M_y/M_s$ signal in the positive direction (point *II*), indicate the occurrence of a switching process associated to the nucleation of new domains; in order to interpret simultaneously the measured values of $M_x$ and $M_y$, also considering the results of the micromagnetic simulations, we have to conclude that transverse magnetic domains form with resultant magnetisation directed along the [010] MgO direction. As sshown in the figure, the $M_x$ and $M_y$ signals can be well interpreted by an asymmetric closed-flux domain configuration, with the positive transverse domain larger than the negative one (the asymmetry is determined by the tilt direction of the applied field, $+5°$).

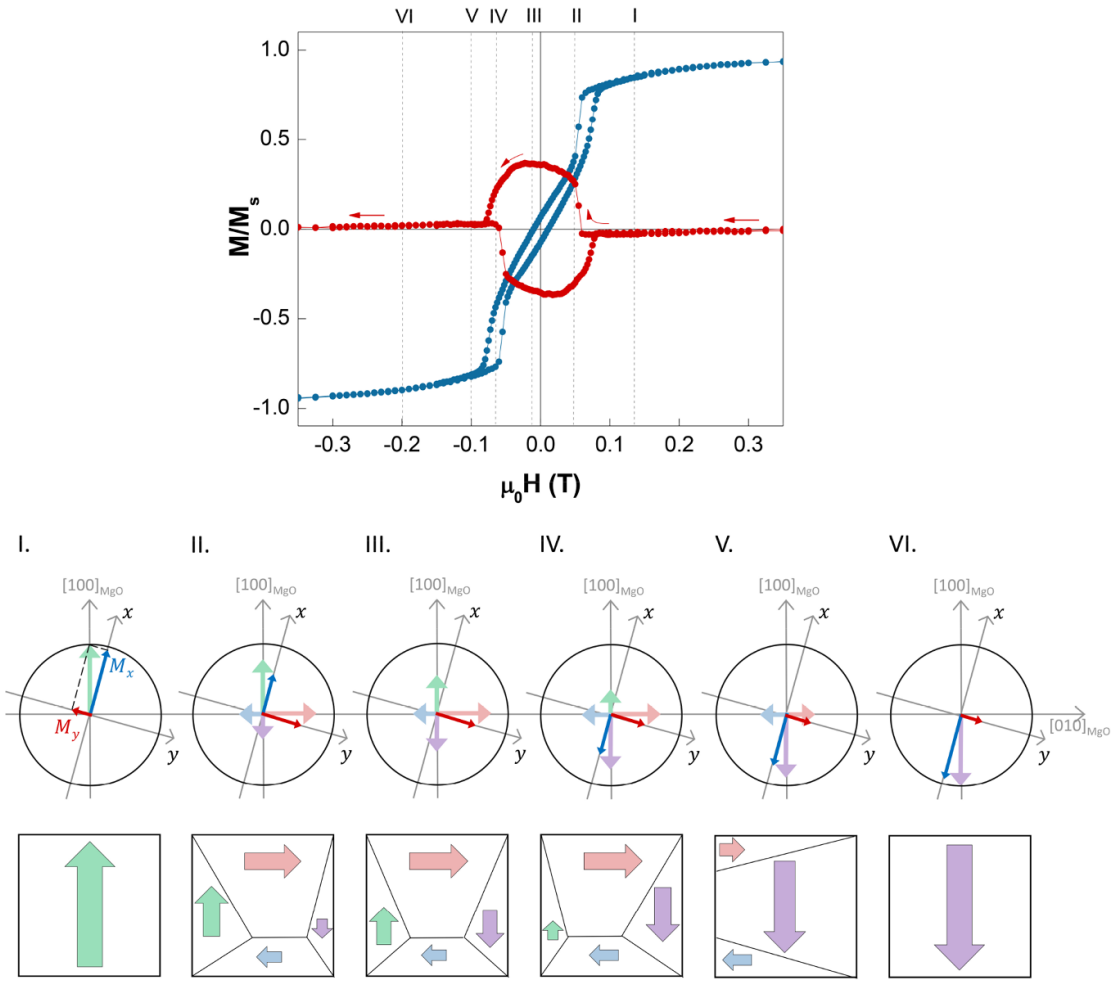


**Figure 7.** (Upper panel) Experimental field-dependent magnetisation loops (M vs H) measured with external field applied at $\theta = +5°$ to the [100] MgO axis. Both the parallel ($M_x/M_s$, blue curve) and transverse ($M_y/M_s$, red curve) magnetisation components are reported. (Middle panel) Qualitative sketches of geometrical arrangement of the magnetisation components along the positive $[100]_{MgO}$ (light green), negative $[100]_{MgO}$ (light violet), positive $[010]_{MgO}$ (light red), negative $[010]_{MgO}$ (light blue) and their resultant projections along the x (blue) and y (red) directions corresponding to representative points (from I to VI) indicated in the M vs H loops. (Bottom panel) Corresponding magnetic domain configurations at the representative points marked in the M vs H loops (from I to VI). The relative lengths of the arrows in both the middle and bottom panel are only qualitative and were set with the aim of showing the evolution of the magnetization components along different directions.

Further sweeping the external field towards lower and then negative values (points *III*) results in an increase of magnetic domains oriented along the negative MgO [100] direction at the expense of those oriented along the positive [100] direction, while the transverse magnetic domains are not significantly affected. This justifies both the gradual variation of the $M_x$ signal and the negligible change of the $M_y$ in the central part of the loop. The difference from the simulated curves, where the transverse signal is equal to zero in the same part of the loop, can be likely due to the presence of inhomogeneities (not considered in the simulation) that sustain the formation of the asymmetric closed-flux configuration dominated by transverse magnetic domains oriented along the positive [010] MgO direction. The same conclusion can be drawn by comparing the experimental and simulated $M_x$ signals.

The steep change of the $M_x$ signal around point *IV* suggests a sudden increase of the magnetic domains oriented along the negative [100] MgO direction at the expense of the transverse domains, which leads to a simultaneous reduction of the $M_y$ signal. By further increasing the external field (from point *V* to *VI*), the transverse magnetic domains further reduce, and the magnetic moments are mainly oriented along the negative [100] MgO direction. Finally, the moments rotate along the field direction as the field strength increases towards the saturation point, thus explaining the gradual increase of the $M_x$ component and the corresponding decrease of the $M_y$ signal.

As a further step to improve the comprehension of magnetisation processes in magnetic shape memory thin films, we have extended the comparison between micromagnetic model and experimental magnetisation curves to a film with a different type of microstructure, *i.e.* a film with Y-type twin lamellae oriented along two orthogonal directions corresponding to the [100] and [010] directions of the MgO

substrate. The results are reported in the supplementary material (figure S4) and confirm the good agreement between magnetometry and micromagnetic results. This specific microstructure resembles the one assumed in [36], but with two areas for each orientation of the Y-type variants instead of one only.

For Y-type twin microstructure, and for the two kinds of twin variant orientations that we have investigated, a pure micromagnetic model is able to give a clear and consistent interpretation of the experimental magnetisation curves and of magnetic microscopy results. The magnetisation jumps occurring when the magnetic field is applied along the alignment directions of Y-type twin boundaries also appear in the simulated curves, showing that the spatial organisation of magnetocrystalline anisotropy axes originated by twinning can give rise to steep magnetisation variations similar to those associated to the MIR effect in bulk single crystals. The magnetic domain configuration shown by micromagnetic simulations explains some of the details of transverse magnetisation measurements and also of previously reported magnetic microscopy results. Further progress towards understanding shape memory effects in Ni–Mn–Ga films could be made by modelling the specific twin microstructures occurring in epitaxial thin films with including also the structural and magnetostructural energy terms in the free energy, as done in [46, 47] with the aim of modelling the general magneto-mechanical behaviour of magnetic shape-memory alloys.

## 4. Conclusions

We have investigated, in-depth, the magnetisation process of a 200 nm martensitic Ni–Mn–Ga thin film, showing at RT a Y-type twin microstructure with unidirectional alignment. The study has been carried out by vector magnetometry and micromagnetic modelling, introducing the experimental characteristics in the model, and considering different orientations of the applied field with respect to the symmetry directions of the sample. The comparison has been extended to a thin film showing Y-type twin boundaries with two orthogonal orientations.

The main features of the magnetisation curves measured along the film symmetry directions are well reproduced by the model, which is purely micromagnetic, *i.e.* neglecting structural and magnetostructural contributions to the free energy. The model shows a three-dimensional evolution of the micromagnetic structure during magnetisation reversal, which is consistent with the detailed vector magnetometry characterisation and with magnetic microscopy. The good agreement between experimental results and simulations demonstrates that the spatial organisation of magnetocrystalline anisotropy axes due to martensitic twinning has a dominant effect on the magnetisation process, giving rise to magnetisation jumps when the magnetic field is applied along the alignment direction of Y-type twin boundaries. Along this direction, simulations show that, in order to minimize magnetocrystalline anisotropy and magnetostatic energy, magnetisation reversal proceeds through the formation and three-dimensional expansion of magnetic domains, passing around zero field through a closed-flux domain configuration, in which the domains with resultant opposite magnetisation directions in the film plane are separated by domain walls with perpendicular orientation of the magnetic moments.

## Acknowledgments

The authors are grateful to Paola Tiberto and Federica Celegato (INRIM, Torino, Italy) for the electron microscopy images, and to Luigi Mori for his help in setting up the micromagnetic model.

## ORCID iD

Francesca Casoli https://orcid.org/0000-0002-4323-0362

## References

[1] Faran E and Shilo D 2016 Ferromagnetic shape memory alloys-challenges, applications, and experimental characterization *Exp. Tech.* **40** 1005–1031
[2] Riccardi L, Naso D, Turchiano B and Janocha H 2013 Adaptive control of positioning systems with hysteresis based on magnetic shape memory alloys *IEEE Trans. Control Syst. Technol.* **21** 2011–23
[3] Kohl M, Schmitt M, Backen A, Schultz L, Krevet B and Fähler S 2014 Ni–Mn–Ga shape memory nanoactuation *Appl. Phys. Lett.* **104** 043111
[4] Watson C S, Hollar C, Anderson K, Knowlton W B and Müllner P 2013 Magnetomechanical four-state memory *Adv. Funct. Mater.* **23** 3995–4001
[5] Ullakko K, Huang J K, Kantner C, O'Handley R C and Kokorin V V 1996 Large magnetic-field-induced strains in $Ni_2MnGa$ single crystals *Appl. Phys. Lett.* **69** 1966–8
[6] Chernenko V A, Cesari E, Kokorin V V and Vitenko I N 1995 The development of new ferromagnetic shape memory alloys in Ni–Mn–Ga system *Scr. Metall. Mater.* **33** 1239–44

[7] Heczko O, Scheerbaum N, Gutfleisch O *et al* 2009 Magnetic shape memory phenomena *Nanoscale Magn. Mater. Appl.*, ed J P Liu, E Fullerton, O Gutfleisch and D J Sellmyer (Boston, MA: Springer) pp 399–439

[8] Righi L, Albertini F, Villa E, Paoluzi A, Calestani G, Chernenko V, Besseghini S, Ritter C and Passaretti F 2008 Crystal structure of 7M modulated Ni–Mn–Ga martensitic phase *Acta Mater.* **56** 4529–35

[9] Lanska N, Söderberg O, Sozinov A, Ge Y, Ullakko K and Lindroos V K 2004 Composition and temperature dependence of the crystal structure of Ni–Mn–Ga alloys *J. Appl. Phys.* **95** 8074–8

[10] Pons J, Chernenko V A, Santamarta R and Cesari E 2000 Crystal structure of martensitic phases in Ni–Mn–Ga shape memory alloys *Acta Mater.* **48** 3027–38

[11] Takagi T, Khovailo V, Nagatomo T, Matsumoto M, Ohtsuka M, Abe T and Miki H 2002 Two-way shape memory effect and mechanical properties of pulse discharge sintered $Ni_{2.18}Mn_{0.82}Ga$ *Int. J. Appl. Electromagn. Mech.* **16** 173–9

[12] Cherechukin A A, Dikshtein I E, Ermakov D I, Glebov A V, Koledov V V, Kosolapov D A, Shavrov V G, Tulaikova A A, Krasnoperov E P and Takagi T 2001 Shape memory effect due to magnetic field-induced thermoelastic martensitic transformation in polycrystalline Ni–Mn–Fe–Ga alloy *Phys. Lett.* A **291** 175–83

[13] Sozinov A, Likhachev A A, Lanska N and Ullakko K 2002 Giant magnetic-field-induced strain in NiMnGa seven-layered martensitic phase *Appl. Phys. Lett.* **80** 1746–8

[14] Murray S J, Marioni M, Allen S M, O'Handley R C and Lograsso T A 2000 6% magnetic-field-induced strain by twin-boundary motion in ferromagnetic Ni–Mn–Ga *Appl. Phys. Lett.* **77** 886–8

[15] Sozinov A, Lanska N, Soroka A and Zou W 2013 12% magnetic field-induced strain in Ni–Mn–Ga-based non-modulated martensite *Appl. Phys. Lett.* **102** 021902

[16] Kohl M, Brugger D, Ohtsuka M and Krevet B 2007 A ferromagnetic shape memory actuator designed for large 2D optical scanning *Sensors Actuators* A **135** 92–98

[17] Gueltig M, Wendler F, Ossmer H, Ohtsuka M, Miki H, Takagi T and Kohl M 2016 High-performance thermomagnetic generators based on Heusler alloy films *Adv. Energy Mater.* **7** 1601879

[18] Lambrecht F, Lay C, Aseguinolaza I R, Chernenko V and Kohl M 2016 NiMnGa/Si shape memory bimorph nanoactuation *Shape Mem. Superelasticity* **2** 347–59

[19] Backen A, Yeduru S R, Diestel A, Schultz L, Kohl M and Fähler S 2012 Epitaxial Ni–Mn–Ga films for magnetic shape memory alloy microactuators *Adv. Eng. Mater.* **14** 696–709

[20] Dong J W, Xie J Q, Lu J, Adelmann C, Palmstrøm C J, Cui J, Pan Q, Shield T W, James R D and McKernan S 2004 Shape memory and ferromagnetic shape memory effects in single-crystal $Ni_2MnGa$ thin films *J. Appl. Phys.* **95** 2593–600

[21] Jenkins C A, Ramesh R, Huth M, Eichhorn T, Pörsch P, Elmers H J and Jakob G 2008 Growth and magnetic control of twinning structure in thin films of Heusler shape memory compound $Ni_2MnGa$ *Appl. Phys. Lett.* **93** 234101

[22] Eichhorn T, Hausmanns R, Klaer P, Kallmayer M, Elmers H-J and Jakob G 2012 Structure and microscopic magnetism of epitaxial Ni–Mn–Ga films *Adv. Eng. Mater.* **14** 687–95

[23] Sharma A, Mohan S and Suwas S 2016 Structural, microstructural and magnetic investigations on the epitaxially grown $Ni_2MnGa(010)$ films on MgO(100) substrate *Intermetallics* **77** 6–13

[24] Thomas M, Heczko O, Buschbeck J, Rößler U K, McCord J, Scheerbaum N, Schultz L and Fähler S 2008 Magnetically induced reorientation of martensite variants in constrained epitaxial Ni–Mn–Ga films grown on MgO(001) *New J. Phys.* **10** 023040

[25] Aseguinolaza I R, Golub V, Salyuk O Y, Muntifering B, Knowlton W B, Müllner P, Barandiarán J M and Chernenko V A 2016 Self-patterning of epitaxial Ni–Mn–Ga/MgO(001) thin films *Acta Mater.* **111** 194–201

[26] Ranzieri P *et al* 2015 Achieving giant magnetically induced reorientation of martensitic variants in magnetic shape-memory Ni–Mn–Ga films by microstructure engineering *Adv. Mater.* **27** 4760–6

[27] Sharma A, Mohan S and Suwas S 2019 Evidence of adaptive modulation and magnetic field induced reorientation of variants in epitaxially grown Ni–Mn–Ga thin film on $Al_2O_3$ (112 – 0) substrate *Mater. Sci. Eng.* B **242** 6–16

[28] Heczko O, Thomas M, Buschbeck J, Schultz L and Fähler S 2008 Epitaxial Ni–Mn–Ga films deposited on $SrTiO_3$ and evidence of magnetically induced reorientation of martensitic variants at room temperature *Appl. Phys. Lett.* **92** 072502

[29] Ranzieri P, Fabbrici S, Nasi L, Righi L, Casoli F, Chernenko V A, Villa E and Albertini F 2013 Epitaxial Ni–Mn–Ga/MgO(100) thin films ranging in thickness from 10 to 100nm *Acta Mater.* **61** 263–72

[30] Yang B, Li Z B, Zhang Y D, Qin G W, Esling C, Perroud O, Zhao X and Zuo L 2013 Microstructural features and orientation correlations of non-modulated martensite in Ni–Mn–Ga epitaxial thin films *Acta Mater.* **61** 6809–20

[31] Niemann R, Backen A, Kauffmann-Weiss S, Behler C, Rößler U K, Seiner H, Heczko O, Nielsch K, Schultz L and Fähler S 2017 Nucleation and growth of hierarchical martensite in epitaxial shape memory films *Acta Mater.* **132** 327–34

[32] Heczko O 2005 Magnetic shape memory effect and magnetization reversal *J. Magn. Magn. Mater.* **290–1** 787–94

[33] Neudert A, Lai Y W, Schäfer R, Kustov M, Schultz L and McCord J 2012 Magnetic domains and twin boundary movement of NiMnGa magnetic shape memory crystals *Adv. Eng. Mater.* **14** 601–613.

[34] Xie R, Tang S-L, Tang Y-M, Liu X-C, Tang T and Du Y-W 2013 Transformation behaviors, structural and magnetic characteristics of Ni–Mn–Ga films on MgO (001) *Chin. Phys.* B **22** 107502

[35] Diestel A, Neu V, Backen A, Schultz L and Fähler S 2013 Magnetic domain pattern in hierarchically twinned epitaxial Ni–Mn–Ga films *J. Phys.: Condens. Matter.* **25** 266002

[36] Laptev A, Lebecki K, Welker G, Luo Y, Samwer K and Fonin M 2016 Origin of steps in magnetization loops of martensitic Ni–Mn–Ga films on MgO(001) *Appl. Phys. Lett.* **109** 132405

[37] Jakob A M, Hennes M, Müller M, Spemann D and Mayr S G 2013 Coupling of micromagnetic and structural properties across the martensite and Curie temperatures in miniaturized Ni–Mn–Ga ferromagnetic shape memory alloys *Adv. Funct. Mater.* **23** 4694

[38] Phatak C, Heinonen O, De Graef M and Petford-Long A 2016 Nanoscale skyrmions in a nonchiral metallic multiferroic: $Ni_2MnGa$ *Nano Lett.* **16** 4141–8

[39] Takhsha Ghahfarokhi M *et al* 2020 Martensite-enabled magnetic flexibility: the effects of post-growth treatments in magnetic-shape-memory Heusler thin films *Acta Mater.* **187** 135–45

[40] Donahue M J and Porter D G 1999 *OOMMF User's Guide, Version 1.0* (Gaithersburg, MD: National Institute of Standards and Technology) (https://doi.org/10.6028/NIST.IR.6376)

[41] Albertini F, Solzi M, Paoluzi A and Righi L 2008 Magnetocaloric properties and magnetic anisotropy by tailoring phase transitions in NiMnGa alloys *Mater. Sci. Forum.* **583** 169–96

[42] Pramanick A *et al* 2015 Direct in situmeasurement of coupled magnetostructural evolution in a ferromagnetic shape memory alloy and its theoretical modeling *Phys. Rev.* B **92** 134109

[43] Thomas M, Heczko O, Buschbeck J, Lai Y W, McCord J, Kaufmann S, Schultz L and Fähler S 2009 Stray-field-induced actuation of free-standing magnetic shape-memory films *Adv. Mater.* **21** 3708–11
[44] Kaufmann S, Niemann R, Thersleff T, Rößler U K, Heczko O, Buschbeck J, Holzapfel B, Schultz L and Fähler S 2011 Modulated martensite: why it forms and why it deforms easily *New J. Phys.* **13** 053029
[45] Hubert A and Schäfer R 1998 *Magnetic Domains: The Analysis of Magnetic Microstructures* (Berlin: Springer) (https://doi.org/10.1007/978-3-540-85054-0)
[46] Gebbia J F, Lloveras P, Castán T, Saxena A and Planes A 2015 Modelling shape-memory effects in ferromagnetic alloys *Shape Mem. Superelasticity* **1** 347–58
[47] Chen X, Moumni Z, He Y and Zhang W 2014 A three-dimensional model of magneto-mechanical behaviors of martensite reorientation in ferromagnetic shape memory alloys *J. Mech. Phys. Solids* **64** 249–86